Progress In Electromagnetics Research B, Vol. 60, 301–315, 2014

Ducting and Turbulence Effects on Radio-Wave Propagation in an Atmospheric Boundary Layer

Yung-Hsiang Chou and Jean-Fu Kiang*

Abstract—The split-step Fourier (SSF) algorithm is applied to simulate the propagation of radio waves in an atmospheric duct. The refractive-index fluctuation in the ducts is assumed to follow a two-dimensional Kolmogorov power spectrum, which is derived from its three-dimensional counterpart via the Wiener-Khinchin theorem. The measured profiles of temperature, humidity and wind speed in the Gulf area on April 28, 1996, are used to derive the average refractive index and the scaling parameters in order to estimate the outer scale and the structure constant of turbulence in the atmospheric boundary layer (ABL). Simulation results show significant turbulence effects above sea in daytime, under stable conditions, which are attributed to the presence of atmospheric ducts. Weak turbulence effects are observed over lands in daytime, under unstable conditions, in which the high surface temperature prevents the formation of ducts.

1. INTRODUCTION

There are three basic types of atmospheric duct: Surface duct, surface-based duct and elevated duct. A surface duct is usually caused by a temperature inversion [1]. An evaporation duct is a special case of surface duct, which appears over water bodies accompanied by a rapid decrease of humidity with altitude [2]. Surface-based ducts are formed when the upper air is exceptionally warm and dry compared with that on the surface [2]. Elevated ducts usually appear in the trade-wind regions between the mid-ocean high-pressure cells and the equator [2].

Non-standard tropospheric refraction may create a ducting, which can bend the surface-based radar beams from the anticipated direction [3]. Ducting may also affect radio communications links [4, 5], or falsely extend the apparent radar range of a target on or near the sea surface [2].

Ducts are frequently observed in the coastal areas where the horizontal variation of refractive-index can not be ignored. In [6], a range-independent surface-based duct has been compared with a mixed land-sea path, using two M-profiles.

In these ducting environments, the wave equation can be approximated by a parabolic equation (PE), which can then be solved using numerical techniques like the split-step Fourier (SSF) [7], finite difference [8], or finite element algorithm [9]. The SSF algorithm is numerically stable and allows a larger step size in the propagation direction, making it suitable to compute the field distribution over long ranges. The PE model appears to provide a fair estimation of path-related parameters over a wide range of frequencies (X, Ka and W bands) and a variety of atmospheric conditions [10].

Turbulent motions in an atmospheric boundary layer (ABL) are driven primarily by the wind shear in the layer and the solar heating on the bottom surface [11]. The effects of air turbulence has been studied by applying a perturbation technique in a mode theory [12], or applying a phase-screen method in an SSF model [13, 14]. The results of different models have been compared over a series of over-water

Received 22 June 2014, Accepted 21 August 2014, Scheduled 26 August 2014

* Corresponding author: Jean-Fu Kiang (jfkiang@ntu.edu.tw).

The authors are with the Department of Electrical Engineering, Graduate Institute of Communication Engineering, National Taiwan University, Taipei 106, Taiwan, R.O.C..

measurements, in a nearly standard atmosphere [14]. When the turbulence effect is included in the model, matching with the measured data has always been improved, especially at higher frequencies.

By including rough sea surface, the modeled data become closer to the measured data [15]; but the path-loss is still underestimated by 3 to 12 dB, partly attributed to the turbulence. Monte-Carlo simulations have been used to study the scattering properties of scalar waves in randomly fluctuating slabs with an exponential spatial correlation, as well as non-exponential spatial correlations [16, 17].

The scaling approach is often used to describe the turbulence in an atmospheric boundary layer (ABL), which is divided into various regions, with each characterized by different scaling parameters. Thus, the structure of an ABL can be described in terms of only a few characteristic parameters. The validity of the scaling approach has been confirmed by experiments and by numerical simulations, under unstable and stable ABL [18–21].

In this work, the SSF algorithm is applied to simulate the wave propagation over a long horizontal range. Monte-Carlo simulations are used to generate profiles of refractive-index fluctuation in the atmosphere, and the scaling approach is used to model the structure of the ABL. The relevant models are described in Section 2, the proper ranges of parameters involved in these models are evaluated in Section 3, simulation results of practical atmospheric ducts are presented and discussed in Section 4. Finally, some conclusions are drawn in Section 5.

2. CONSTRUCTION OF MODELS

2.1. Propagation Model

Under the paraxial approximation that the wave predominantly propagates in the horizontal ($\hat{x}$) direction, the Helmholtz wave equation reduces to the parabolic equation [7]

$$\frac{\partial u(x,z)}{\partial x} \simeq j\left\{\frac{k}{2}\left[m^2(x,z)-1\right]+\frac{1}{2k}\frac{\partial^2}{\partial z^2}\right\}u(x,z) \tag{1}$$

where x is the propagation range, z the height above the Earth surface, k the wavenumber in free space, $m = 1 + M \times 10^{-6}$, and the modified refractivity M is related to the refractivity N as $M = N + 0.157z$. Eq. (1) gives fairly accurate solution when the propagation angle is within 15° of the horizontal direction [22].

The split-step solution to (1) can be expressed as [7]

$$u(x+\Delta x,z) = e^{j(k/2)(m^2-1)\Delta x}\mathcal{F}^{-1}\left\{e^{-j(p^2/2k)\Delta x}\mathcal{F}\{u(x,z)\}\right\} \tag{2}$$

where $p = k\sin\xi$ is the vertical phase constant and ξ the angle off the horizontal direction. The solution, $u(x,z)$, and its spectrum, $U(x,p)$, are related by the Fourier transform $\mathcal{F}\{\cdot\}$ and its inverse $\mathcal{F}^{-1}\{\cdot\}$ as

$$\mathcal{F}\{u(x,z)\} = \frac{1}{\sqrt{2\pi}}\int_{-\infty}^{\infty} u(x,z)e^{jpz}dz$$

$$\mathcal{F}^{-1}\{U(x,p)\} = \frac{1}{\sqrt{2\pi}}\int_{-\infty}^{\infty} U(x,p)e^{-jpz}dp$$

The path-loss (PL) is defined as [22]

$$\mathrm{PL} = 20\log_{10}\frac{4\pi\sqrt{x}}{\lambda^{3/2}|u(x,z)|}\ (\mathrm{dB}) \tag{3}$$

where λ is the wavelength in free space.

The field distribution in the cross section of the transmitting site can be approximated by a Gaussian distribution as [5]

$$u(0,z) = \frac{1}{\sqrt{\pi}B}e^{-jk\sin\theta_e z}e^{-(z-z_t)^2/B^2}$$

where $B = \sqrt{2\ln 2}/[k\sin(\theta_{bw}/2)]$, z_t is the height of the transmitting antenna, θ_e the elevation angle measured from the transmitting antenna, and θ_{bw} the 3 dB beamwidth of its radiation pattern.

Figure 1 shows the computational domain of the SSF method, where the reflected field is accounted for by including an image source. The field is artificially attenuated smoothly in an extended adsorption zone by imposing a window function.

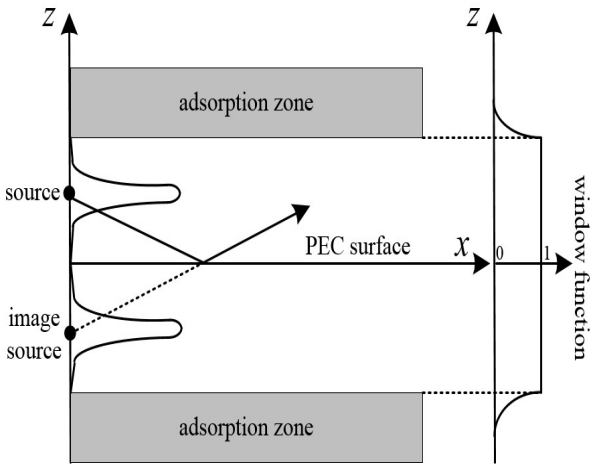

Figure 1. Computational domain including an image source and imposed with a window function.

2.2. Refractive-index Fluctuation

The total refractive index can be decomposed as

$$n(x,z) = \hat{n}(z) + n_f(x,z) \tag{4}$$

where $\hat{n}(z)$ is the average refractive index and $n_f(x,z)$ the refractive-index fluctuation. A two-dimensional version of the latter can be realized with Monte-Carlo simulation as [16, 23]

$$n_f^{(s)}(x,z) = \sum_{p=1}^{\infty}\sum_{q=1}^{\infty} a_{pq}^{(s)} \sin\left(\zeta_{xp}x + \zeta_{zq}z\right) + b_{pq}^{(s)} \cos\left(\zeta_{xp}x + \zeta_{zq}z\right) \tag{5}$$

where s is the realization index, ζ_{xp} the pth wavenumber, and a_{pq} and b_{pq} are random numbers with variance σ_{pq}^2, which can be expressed as $\sigma_{pq}^2 = 4\Delta\zeta_{xp}\Delta\zeta_{zq}F_n(\zeta_{xp},\zeta_{zq})$, where $F_n(\zeta_x,\zeta_z)$ is the two-dimensional power spectral density of the refractive-index fluctuation.

By applying the Wiener-Khinchin theorem [24], the two-dimensional power spectral density of an isotropic Kolmogorov turbulence can be derived from its three-dimensional counterpart as [25]

$$F_n^{\mathrm{K}}(\zeta_x,\zeta_z) = \frac{0.0555C_n^2}{\left(\zeta_x^2 + \zeta_z^2 + 1/L_0^2\right)^{4/3}} \tag{6}$$

where L_0 is the outer scale, and C_n^2 is the structure constant. A two-dimensional anisotropic Kolmogorov spectrum can be modified from (6) as [25]

$$F_n^{\mathrm{K}}(\zeta_x,\zeta_z) = \frac{0.0555C_n^2(L_{0x}L_{0z})^{4/3}}{\left(\zeta_x^2L_{0x}^2 + \zeta_z^2L_{0z}^2 + 1\right)^{4/3}} \tag{7}$$

where L_{0z} and L_{0x} are the outer scales in the vertical and the horizontal directions, respectively.

The constraint of applying a 2D propagation scheme to predict 3D turbulence effects has been discussed [26]. The phase variance of the 2D model is slightly overestimated. The log-amplitude variances of 3D and 2D models agree well in the Fraunhofer region, but the 2D model tends to underestimate the variance in the Fresnel region.

3. ESTIMATION OF PARAMETERS

The refractivity (N) of the atmosphere at microwave frequencies is related to the refractive index (n) as $n = 1 + N \times 10^{-6}$. It can be empirically estimated as $N = (77.6/T)(P + 4810e/T)$ [27, 28], where T is the absolute temperature (in K), $P = P_d + e$ is the atmospheric pressure (in hPa), P_d is the dry-air

pressure, and e is the water vapor pressure (in hPa). The modified refractivity (M) is related to N as $M = N + 10^6 \times z/R_e$ [2], where $R_e = 6.371 \times 10^6$ (m) is the mean Earth radius, and z (m) is the height above the Earth surface.

The dry-air pressure can be derived from barometric formula, $P_d = P_0 e^{-gmz/(RT_0)}$ [29], where $P_0 = 1013.25$ (in hPa) is the standard reference pressure, $g = 9.8$ (in m/s^2) is the acceleration of gravity, $m = 0.0289644$ (in kg/mol) is the molar mass of dry air, $R = 8.31447$ (in J/mol/K) is the ideal gas constant, and T_0 (in K) is the temperature at sea level.

The water vapor pressure (e) is related to the humidity mixing ratio (Q) (in g/kg) as $e = QP_d/622$ [30]. The potential temperature (θ) is defined as $\theta = T(P_0/P)^{R/c_p}$ [31], where $R = 287.04$ (in J/K/kg) is the ideal gas constant of dry air, and $c_p = 1005$ (in J/K/kg) is the specific heat capacity of dry air under a constant pressure, $R/c_p \simeq 0.286$.

3.1. Scaling Approach on ABL's

The scaling approach has been used to describe the turbulence in the atmospheric boundary layer (ABL) [18], with the ABL divided into several regions, each characterized by a set of scaling parameters. Fig. 2 shows the idealized scaling regions, in an unstable ABL ($L_{\rm mo} < 0$) and a stable ABL ($L_{\rm mo} > 0$), respectively [18]. The major scaling parameters in each region are listed in the parentheses, assuming that the ABL is horizontally homogeneous, without clouds or fogs.

The Monin-Obukhov length ($L_{\rm mo}$) is a scaling parameter for characterizing the surface layer; the local Monin-Obukhov length (Λ) is a local scaling parameter for characterizing the stratification phenomenon above the surface layer in a stable ABL; u_* is the velocity scale of the friction velocity, u_{*0} is the friction velocity in the surface layer, which is nearly independent of height; and w_* is the convective velocity scale in an unstable ABL.

The shear-dominated surface layers, $0.01 < z/h < 0.1$, $-z/L_{\rm mo} < 0.5$, $-h/L_{\rm mo} < 5 \sim 50$ in Fig. 2(a) and $z/h < 0.1$, $h/L_{\rm mo} < 10$, $z/\Lambda < h/\Lambda - 10$ in Fig. 2(b), can be characterized by the Monin-Obukhov similarity theory, with the parameters u_{*0}, z and $L_{\rm mo}$. The curve, $z/\Lambda = h/\Lambda - 10$, divides the z-less scaling layer and the intermittency layer. The local Monin-Obukhov length is related to $L_{\rm mo}$ as $\Lambda = L_{\rm mo}(1 - z/h)^{\alpha_3}$, where α_3 is an empirical parameter.

In Fig. 2(a), the ABL to the right of the dashed line, $-z/L_{\rm mo} \simeq 0.5$, is driven to a convective state. When $-z/L_{\rm mo} > 1$, the convective process dominates, leading to a free convection layer ($0.01 < z/h < 0.1$) or a mixed layer ($0.1 < z/h < 0.8$). The characteristics of a mixed layer becomes independent of $-h/L_{\rm mo}$ once the ABL is driven into the convective state ($-z/L_{\rm mo} > 0.5$). A near-neutral upper layer ($0.1 < z/h < 0.8$, $-z/L_{\rm mo} < 1$) appears over land under low solar insolation or strong winds, and is frequently observed above the sea. In the entrainment layer ($-h/L_{\rm mo} > 1$,

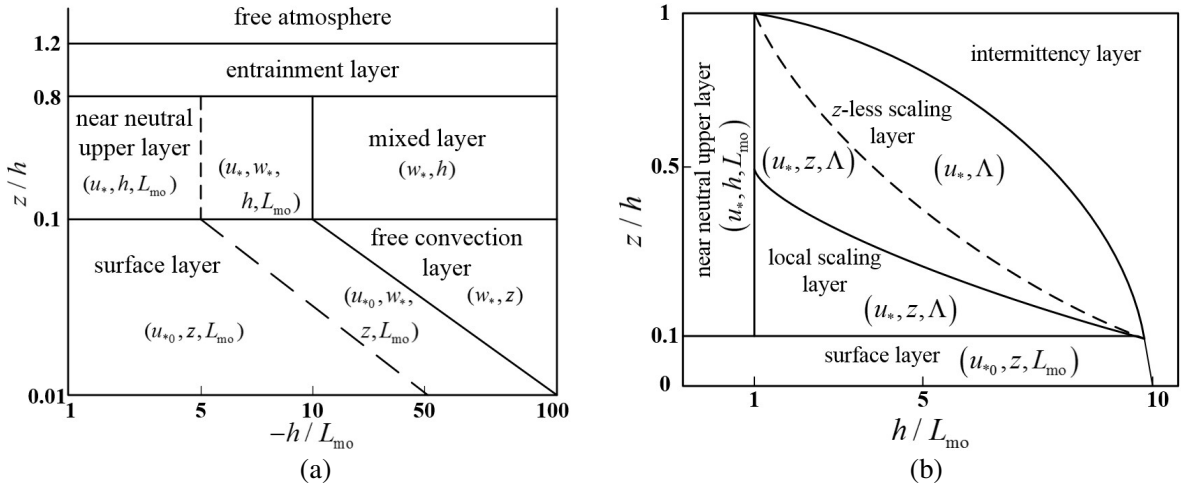

Figure 2. Idealized scaling regions in (a) an unstable ABL and (b) a stable ABL [18, 32].

$0.8 < z/h < 1.2$), the turbulent structure is affected by the atmosphere above the ABL.

A stable ABL can form over land during night-time when the surface is cooled via long-wavelength emission. It can also form over sea via advection of warm air. Under stable conditions, the turbulence of mechanical origin is suppressed by a negative heat flux on the surface. The thickness of boundary layer (h) is typically an order of magnitude smaller than that under unstable conditions.

In a stable ABL, the stratification process leads to small eddies, with smaller outer scale compared to that in a neutral or unstable ABL. Although the structure of a stable ABL is quite different from that of an unstable ABL, the turbulence in the surface layer can still be described with the Monin-Obukhov similarity theory with parameters u_{*0}, z and L_{mo}.

The local Monin-Obukhov length can be applied when $h/L_{\mathrm{mo}} > 1$ and $z/h > 0.1$, in which the turbulent variables are expressed in terms of z/Λ. As shown in Fig. 2(b), the boundary between the local scaling layer and the z-less scaling layer appears around $z/\Lambda = 1$. As z/Λ becomes larger, the dependence on z becomes weaker and finally disappears beyond $z/L_{\mathrm{mo}} = 1$ (dashed line), in which case the eddies are reduced in size and their vertical motion is inhibited by the stabilizing stratification. The turbulent eddies stop being affected by the surface, and the dimensionless quantities, like Richardson number, approach constant values. This phenomenon is called z-less stratification.

In the intermittency layer ($z/\Lambda > h/\Lambda - 10$) shown in Fig. 2(b), the turbulence becomes very weak and sporadic, no longer continuous in time and space. The intermittency layer is expected to touch the surface at low wind speed or high stability.

Continuous turbulence may appear at relatively small h/L_{mo}. The z-less region may expand with h/L_{mo}, up to $h/L_{\mathrm{mo}} \simeq 5$, then is restrained by the intermittency layer from above.

3.2. Monin-Obukhov Length

The Monin-Obukhov length is defined as [33]

$$L_{\mathrm{mo}} = \frac{T_0}{g k_a} \frac{u_{*0}^2}{\theta_{*0}} \tag{8}$$

where $g = 9.8$ (m/s^2) is the acceleration of gravity, $k_a = 0.4$ is the von Karman constant, T_0 (K) is the reference temperature; u_{*0} and θ_{*0} are the friction velocity and the temperature scales, respectively, near the surface.

The Monin-Obukhov length is essentially determined by the heat flux and the friction velocity, which are nearly independent of height within the surface layer. The atmosphere can be generally characterized in terms of z/L_{mo} as follows [34]: When z/L_{mo} is a large negative number, the heat convection dominates. When z/L_{mo} is a small negative number, the mechanical turbulence dominates. When $z/L_{\mathrm{mo}} = 0$, only mechanical turbulence contributes. When z/L_{mo} is a small positive number, the mechanical turbulence is slightly damped by the temperature stratification. When z/L_{mo} is a large positive number, the mechanical turbulence is severely reduced by the temperature stratification. In summary, z/L_{mo} quantifies the relative significance between heat convection and mechanical turbulence during the day-time, and to what extent the stratification suppresses the mechanical turbulence during the night-time.

3.3. Height of Boundary Layer

The height of the boundary layer (h) also known as the mixing height, is not uniquely defined. In [35], it is defined as the height of the layer adjacent to the ground over which pollutants or similar substances emitted within this layer or entrained into it become vertically dispersed by convection or mechanical turbulence, within a time scale of about an hour.

In the entrainment layer of a typical convective boundary layer (CBL), the constituents are not well mixed and the turbulence intensity declines towards its top surface [36, 37]. The thickness of the entrainment layer is typically 30% of the mixed layer. Another definition of the convective mixing height is the height where the heat flux gradient reverses its sign.

A stable boundary layer (SBL) can be divided into two sublayers, a layer of continuous turbulence and an outer layer of sporadic or intermittent turbulence. Under very stable conditions, the layer of sporadic turbulence may extend to the ground, as shown in Fig. 2(b) [18]. The scaling height of an SBL

generally refers to the layer of continuous turbulence since it is very difficult to measure sporadic or intermittent turbulence. Similar to the CBL, the turbulence is not strictly confined to the region below h.

A neutral boundary layer is formed when the heat flux approaches zero, under either stable or unstable condition. The wind shear is the main source of turbulence, and the neutral boundary layer may extend above the ABL.

The boundary layer height can be estimated using empirical formulas derived from measurement or numerical data. Based on the scaling approach, the layer height under stable conditions can be expressed as $h = a_1 L_E = a_1 u_{*0}/f_c$ [35] or $h = a_2\sqrt{L_E L_{\rm mo}} = a_2\sqrt{u_{*0}L_{\rm mo}/f_c}$, where $L_E = u_{*0}/f_c$ is the Ekman length; $a_1 = 0.07$–0.3 and $a_2 = 0.3$–0.7 are empirical coefficients; $f_c = 2\Omega\sin\varphi$ is the Coriolis parameter at latitude φ, with $\Omega = 7.27 \times 10^{-5}$ rad/s, the angular speed of the Earth's rotation. Note that a neutral, stationary boundary layer is assumed, and $1/f_c$ is generally much longer than relevant time scales. In this work, the mixing height of a CBL is estimated as the height where the first potential temperature inversion takes place.

3.4. Structure Constant

The structure constant (C_n^2) usually becomes large near the Earth's surface and in the clouds [38]. The magnitude of C_n^2 generally increases with longer wavelength. It falls, near the ground, in the range of 10^{-16} to 10^{-12} $\mathrm{m}^{-2/3}$ in the visible and the infrared bands [39]; and is orders of magnitude larger in the near-millimeter-wave band than in the infrared.

The structure constant can be estimated using the Kolmogorov-Corrsin formula, $C_n^2 = \beta_n N_n \epsilon^{-1/3}$ [40], where $\beta_n = 2.8$ is the Kolmogorov constant [25], and ϵ is the dissipation rate of the turbulent kinetic energy (TKE). The outer scale of the turbulence in direction i (L_{0i}) can be estimated from the eddy diffusivity (K_i) and the TKE dissipation rate (ϵ) as $L_{0i} = (K_i/\epsilon^{1/3})^{3/4}$ [25]. Thus, the structure constant can be expressed as [25, 41]

$$C_n^2 \simeq \beta_n \left(\frac{\partial\langle n\rangle}{\partial z}\right)^2 L_{0z}^{4/3} \tag{9}$$

In a marine planetary boundary layer (MPBL), the near-surface turbulence leads to relatively large moisture fluctuation [42], which plays a dominant role, as compared to temperature, in determining C_n^2 in microwave bands and significantly affects C_n^2 in acoustic and optical bands. The over-land simulation shows a larger diurnal variation, but the moisture fluctuation does not play a dominant role. Near the surface, the temperature makes a comparable contribution to C_n^2 in microwave bands, particularly in the afternoon. In the acoustic and optical bands, C_n^2 is primarily determined by the temperature fluctuations.

3.5. Outer Scales of Random Medium

A model of eddy diffusivity, based on the diffusion theory and the Eulerian statistical method [11], can be used in the ABL under all stability conditions, except the very stable cases in which the Monin-Obukhov scaling theory does not apply. The eddy diffusivity in a shear-buoyancy ABL can be expressed as [11]

$$K_i = \sigma_{ib}\ell_{ib} + \sigma_{is}\ell_{is} \tag{10}$$

where σ_{ib}^2 and σ_{is}^2 are the Lagrangian variances of the ith component of the turbulent wind field, due to buoyancy and wind shear, respectively; ℓ_{ib} and ℓ_{is} are the Lagrangian lengths due to buoyancy and wind shear, respectively. The interaction between shear and buoyancy is neglected.

The convective velocity scale, under unstable conditions ($L_{\rm mo} < 0$), can be expressed as [11]

$$w_* = u_{*0}\left(-\frac{h}{k_a L_{\rm mo}}\right)^{1/3} \tag{11}$$

The friction velocity can be expressed as [43]

$$u_* = u_{*0}(1 - z/h)^{\alpha} \tag{12}$$

where α depends on the state of the boundary layer, and $\alpha = 1$ [43] is used in this work.

Under an unstable condition, the surface potential temperature is higher than the air potential temperature, u_* (characterizing the wind-shear effect) and w_* (characterizing air convection) will dominate the air turbulence. Under a stable condition, the surface potential temperature is lower than the air potential temperature, the air turbulence is dominated by u_*, and the stabilizing stratification can be characterized by z/Λ.

The eddy diffusivity in the boundary layer ($z/h \leq 1$), under unstable conditions ($L_{\rm mo} < 0$), can be expressed as

$$K_i^{(u)} = K_{ci}^{(u)} + K_{mi}^{(u)} \tag{13}$$

where $K_{ci}^{(u)} = C_{1i} w_* z$ and $K_{mi}^{(u)} = C_{2i} u_* z$ are the convective and the wind-shear turbulence components, respectively, with

$$\begin{aligned} C_{1z} &= \frac{0.16\left(-0.01h/L_{\rm mo}\right)^{1/2}}{(z/h)\left(1 - e^{-4z/h} - 0.0003e^{8z/h}\right)^{-4/3}} \\ C_{2z} &= 0.4/\left(1 + 15 f_c z/u_{*0}\right)^{4/3} \\ C_{1x} &= 0.1086\left(-0.01h/L_{\rm mo}\right)^{1/2}/(z/h) \\ C_{2x} &= 4.913/\left(1 + 116.7 f_c z/u_{*0}\right)^{4/3} \end{aligned} \tag{14}$$

Figure 3(a) shows the distribution of $K_{cz}^{(u)}/K_{mz}^{(u)}$ (in log scale) on the $-h/L_{\rm mo}$-z/h plane, where the Coriolis term in (14) is ignored. The value of $K_{cz}^{(u)}/K_{mz}^{(u)}$ is roughly a constant in each region labeled in Fig. 2(a).

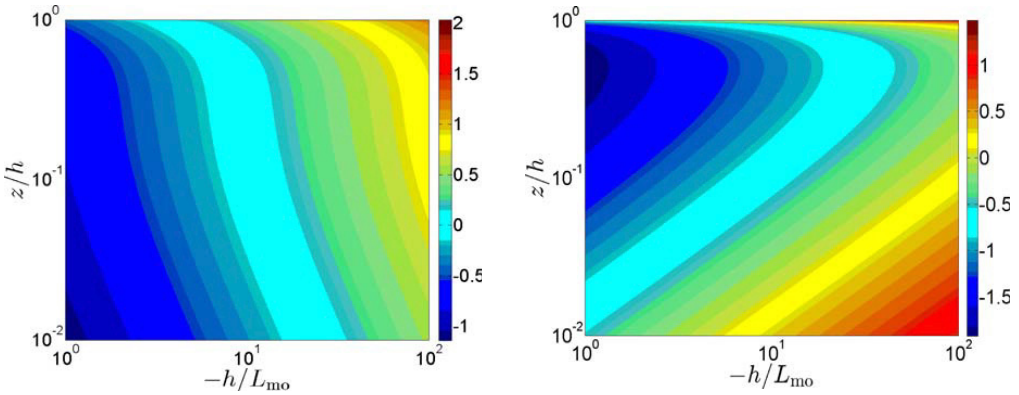

Figure 3. Distribution of (a) $\log_{10}[K_{cz}^{(u)}/K_{mz}^{(u)}]$ and (b) $\log_{10}[K_{cx}^{(u)}/K_{mx}^{(u)}]$ on the $-h/L_{\rm mo}$-z/h plane, in an unstable ABL.

Figure 3(b) shows the distribution of $K_{cx}^{(u)}/K_{mx}^{(u)}$ (in log scale) on the $-h/L_{\rm mo}$-z/h plane. The convective turbulence still dominates as the instability gets stronger, but its influence decreases at higher altitudes in the ABL.

Under stable conditions ($L_{\rm mo} > 0$), on the other hand, we have

$$\begin{aligned} K_z^{(s)} &= \frac{0.4(1 + 3.7z/\Lambda)^{1/3}}{\left(1 + 15 f_c z/u_{*0} + 3.7z/\Lambda\right)^{4/3}} u_* z \\ K_x^{(s)} &= \frac{4.9(1 + 3.7z/\Lambda)^{1/3}}{\left(1 + 116.7 f_c z/u_{*0} + 3.7z/\Lambda\right)^{4/3}} u_* z \end{aligned} \tag{15}$$

Figure 4 shows the distributions of $K_z^{(s)}/(u_{*0}z)$ and $K_x^{(s)}/(u_{*0}z)$ on the $h/L_{\rm mo}$-z/h plane, in which the Coriolis term in (15) is ignored. Both ratios are roughly constant in each region labeled in Fig. 2(b).

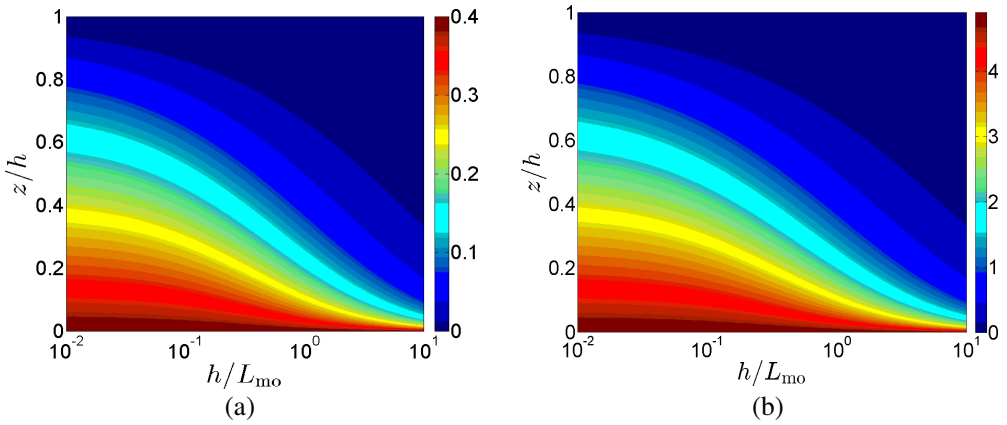

Figure 4. Distribution of (a) $K_z^{(s)}/(u_{*0}z)$ and (b) $K_x^{(s)}/(u_{*0}z)$ on the $h/L_{\rm mo}$-z/h plane in a stable ABL.

The outer scales under unstable conditions ($L_{\rm mo} < 0$) can be expressed as

$$\begin{aligned} L_{0z}^{(u)} &= z\frac{1}{[3.125(1-z/h)^3-1.625z/L_{\rm mo}]^{1/4}}\left\{\frac{0.0217\,(-h/L_{\rm mo})^{5/6}\,(z/h)^{-1}}{\left(1-e^{-4z/h}-0.0003e^{8z/h}\right)^{-4/3}}+\frac{0.4(1-z/h)}{(1+15f_cz/u_{*0})^{4/3}}\right\}^{3/4} \\ L_{0x}^{(u)} &= z\frac{1}{[3.125(1-z/h)^3-1.625z/L_{\rm mo}]^{1/4}}\left\{\frac{0.01474\,(-h/L_{\rm mo})^{5/6}}{(z/h)}+\frac{4.913(1-z/h)}{(1+116.7f_cz/u_{*0})^{4/3}}\right\}^{3/4} \end{aligned} \tag{16}$$

When the convective mechanism dominates the turbulence, as in the free convection layer and the mixed layer labeled in Fig. 2(a), they reduce to

$$\begin{aligned} L_{0cz}^{(u)} &= \frac{0.05\,(-h/L_{\rm mo})^{3/8}}{(z/h)}z\left(1-e^{-4z/h}-0.0003e^{8z/h}\right) \\ L_{0cx}^{(u)} &= \frac{0.0375\,(-h/L_{\rm mo})^{3/8}}{z/h}z \end{aligned} \tag{17}$$

The outer scales, under stable conditions ($L_{\rm mo} > 0$), can be expressed as

$$\begin{aligned} L_{0z}^{(s)} &= \frac{0.3783z}{(1+15f_cz/u_{*0}+3.7z/\Lambda)} \\ L_{0x}^{(s)} &= \frac{2.477z}{(1+116.7f_cz/u_{*0}+3.7z/\Lambda)} \end{aligned} \tag{18}$$

Under strongly stable condition, they reduce to

$$\begin{aligned} L_{0z}^{(s)} &\simeq 0.102L_{\rm mo} \\ L_{0x}^{(s)} &\simeq 0.669L_{\rm mo} \end{aligned} \tag{19}$$

with the anisotropy $L_{0x}^{(s)}/L_{0z}^{(s)} \simeq 6.56$, which is independent of z and consistent with the z-less layer ($\Lambda \simeq L_{\rm mo}$) labeled in Fig. 2(b). Since the turbulence above the ABL is very weak, the outer scales are approximated as zero in this work.

4. SIMULATIONS AND DISCUSSIONS

Simulations will be conducted to compare with the observation data over the Gulf area (50°N, 28°E) on April 28, 1996, which is a typical shamal day, according to the US Navy Ship Antisubmarine Warfare Readiness/ Effectiveness Measuring programme (SHAREM-115) [44, 45].

This case is presented because the data are well validated and involve the whole Gulf orography. Here, shamal means the strong north-westerly winds in this area, which blow frequently in both warm and cold seasons [46]. Shamals are important weather phenomena in the Gulf region as they cause adverse weather conditions, including gusty winds, sand-storms, dust-storms, rough seas, low-level wind shear, and so on. Summer shamals affect the Gulf region predominantly during May to July, and are known to be linked with the seasonal thermal flows over north-west India, Pakistan, Iran and southern Saudi Arabia.

The boundary layer structure over the Gulf is strongly influenced by the surrounding desert landmass. Warm dry air flows from the desert over the relatively cool waters of the Gulf, leading to a stable internal boundary layer. The layer evolves and eventually forms a new marine ABL. The stable stratification tends to suppress vertical mixing and trap moisture within the layer, leading to an increase in refractive index and the formation of a strong atmospheric duct [44].

Ducts form over land and sea at nights. Over the land, ducts are formed by the temperature inversion attributed to radiative cooling near the surface. During the daytime, ducts disappear from the land except the south-east area of the southern Gulf coast, where the air in the convective boundary layer over land is well mixed vertically to create strong gradient of refractive index.

In the air over the waters of the Gulf, the humidity at low-level is high, which sustains the ducts in both time and space. This marine boundary layer (MBL), accompanied by the ambient wind and the land-sea temperature difference of up to 10°C, has the characteristics of a marine internal boundary layer (MIBL) [47]. An MIBL is formed as the air mass moves from a hot dry surface to a cool water surface [44]. The MIBL's are modified by meso-scale structures and diurnal variations [48, 49]. Within about 100 km of the shore, simple surface ducts take shape as a consequence of the increased humidity

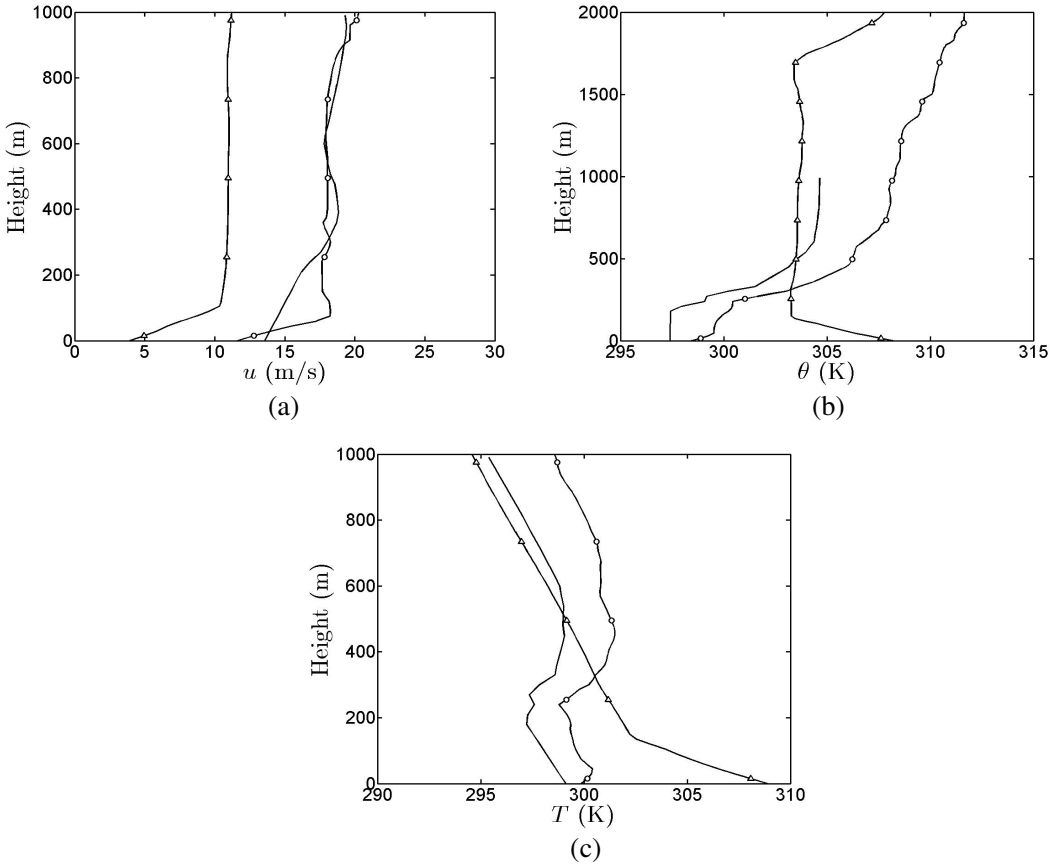

Figure 5. (a) Wind speeds, (b) potential temperature and (c) temperature on April 28, 1996, ——: (27°46'N, 50°45'E) at 1400 UTC (stable ABL), from the control run [45]; —○—: (26°09'N, 53°06'E) at 1330 UTC (stable ABL), from the rawinsonde observation [44]; —△—: (29°13'N, 47°59'E) (Kuwait International Airport) at 1200 UTC (unstable ABL), from the coastal synoptic reporting stations [44].

in the near-surface layer below the temperature inversion height. Beyond 100 km of the shore, further increase of near-surface moisture may transform a surface duct to a surface-based duct. Farther in the downwind direction, the increased cooling at the top of the trapping layer creates a minimum of modified refractivity, with its value larger than that at the surface, and an elevated duct is formed.

Figures 5(a), 5(b) and 6(a) show the measurement data of wind speed (m/s), potential temperature (K) and humidity mixing ratio (g/kg), respectively. Some curves are produced by using the mesoscale model (MM5V3), at the grid size of 25 km, based on the observed data at different locations [45]. Some curves are compiled from the rawinsonde observation and the coastal synoptic reporting stations [44], respectively.

Figure 5(c) shows the temperature profiles derived from the potential temperature in Fig. 5(b) and humidity mixing ratio in Fig. 6(a). Fig. 6(b) shows the profiles of modified refractivity, using the temperature in Fig. 5(c) and the humidity mixing ratio in Fig. 6(a). The curve produced with MM5V3 indicates a ducting layer over the height of 200–350 m. The curve with rawinsonde observation indicates two ducting layers, one below 80 m and the other over 250–300 m.

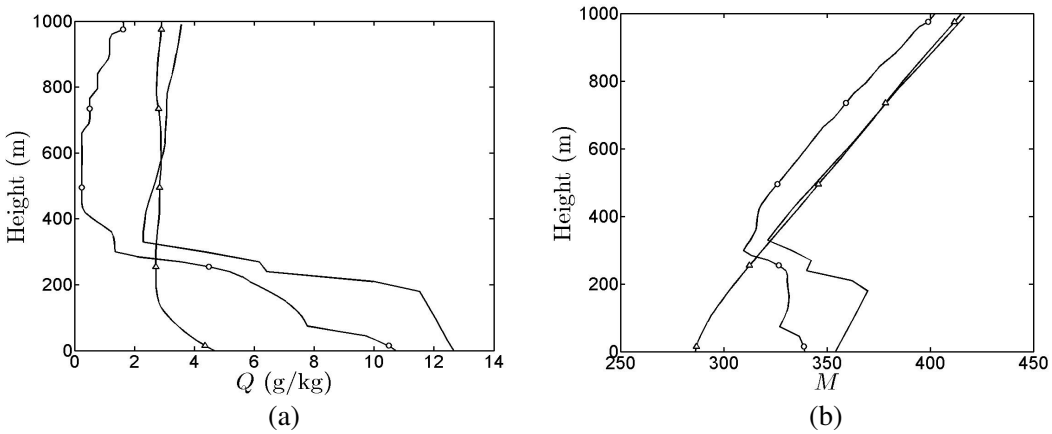

Figure 6. (a) Humidity mixing ratio and (b) modified refractivity, with the same parameters as in Fig. 5.

Table 1 lists the Monin-Obukhov length ($L_{\rm mo}$), the surface friction velocity (u_{*0}), and the surface temperature scale (θ_{*0}), which are derived from the profiles of wind speed in Fig. 5(a) and potential temperature in Fig. 5(b) [44, 45]. The mixing height (h) is derived using the approach described in Section 3.3.

Table 1. Parameters derived from measurements on April 28, 1996 [44, 45].

case	$L_{\rm mo}$ (m)	u_{*0} (m/s)	θ_{*0} (K)	h (m)	latitude (N)	longitude (E)	Time (UTC)
1	407	0.1509	0.0042	288	27°46’	50°45’	1400
2	311	0.8204	0.1643	717	26°09’	53°06’	1330
3	−167	1.3131	−0.8140	1732	29°13’	47°59’	1200

Figures 7(a), 7(b) and 8(a) show the vertical and horizontal outer scales, as well as the anisotropy of outer scales, based on the parameters, $L_{\rm mo}$, h and u_{*0}, listed in Table 1.

The parameters in case 1 of Table 1 are associated with the curves produced with MM5V3. As shown in Fig. 2(b), a near neutral upper layer may appear above the surface layer. Under a near neutral condition (small z/Λ), the horizontal outer scales are significantly reduced, leading to a smaller anisotropy (L_{0x}/L_{0z}). The anisotropy decreases to a minimum in the surface layer, in which the Coriolis term ($f_c z/u_{*0}$) dominates; then increases as the stratification term becomes more important; and may reach a constant at large z/Λ.

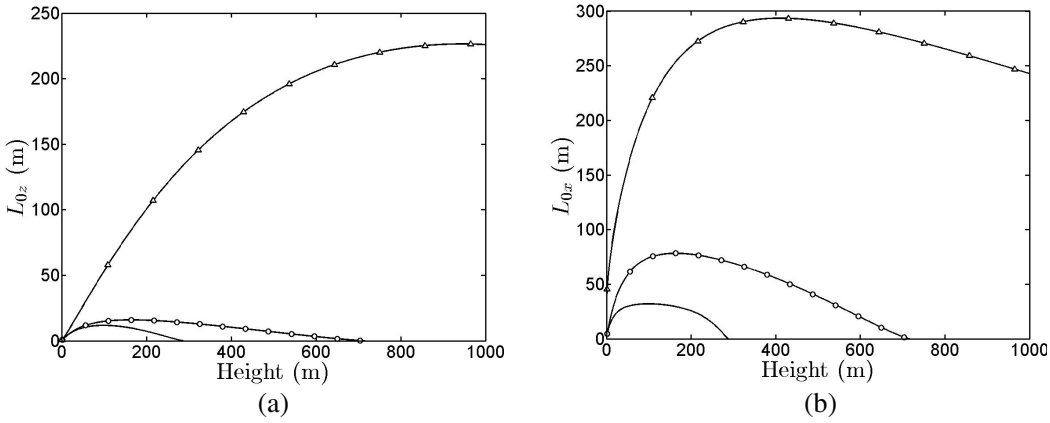

Figure 7. (a) Vertical outer scale and (b) horizontal outer scale, parameters are the same as in Fig. 5.

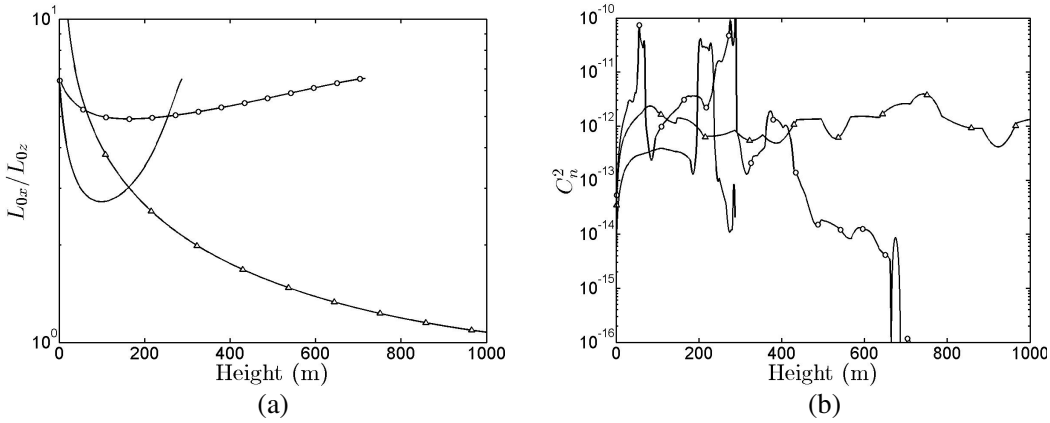

Figure 8. (a) Anisotropy of outer scales and (b) structure constant, parameters are the same as in Fig. 5.

The parameters in case 2 of Table 1 are associated with the rawinsonde curves, representing a more stable condition (large z/Λ). The outer scales (L_{0x} and L_{0z}) are much smaller than those under unstable conditions [50], as shown in Fig. 7. The outer scales under stable conditions are determined by both the Coriolis term (f_c/u_{*0}) and the stratification term (z/Λ). Under a more stable condition, the anisotropy becomes larger due to the vertical compression of air turbulence by a cold surface. It can also be explained using (18), in which the Coriolis term ($f_c z/u_{*0}$) has stronger effect on the horizontal outer scale than on the vertical one. The characteristics of case 2, as shown in Figs. 7 and 8(a), appear more like a z-less layer than a local scaling layer.

In an unstable ABL, the eddies tend to be vertically elongated by convection, leading to a smaller L_{0x}/L_{0z}. The characteristics of case 3 (coastal synoptic curves), with $-h/L_{\rm mo} = -10.4$, appear more like a convective boundary layer as labeled in Fig. 2(a). Note that the horizontal outer scale can be increased by wind shear (u_{*0}), and the vertical outer scale can be increased by high temperature variation (θ_{*0}).

Figure 8(b) shows the structure constant estimated using (9), based on the data of average modified refractivity in Fig. 6(b) and vertical outer scale in Fig. 7(a). In case 3, the structure constant is a relatively smooth function of height, because the vertical outer scale is large and the average modified refractivity is a smooth function of height. However, the structure constant around the ducting region is much smaller than that under stable conditions like cases 1 and 2. Around the ducting region of cases 1 and 2, L_{0z} is relatively small, and the variation of average modified refractivity is relatively large, leading to large C_n^2.

Figures 9 and 10 show the distributions of path-loss in a stable ABL, indicating a surface-based duct and a complex duct, respectively. In Fig. 9, the ducting effect is observed below 300 m. A shadowing

region appears at low altitude around the range of 50 km, indicating a less steady communication channel therein, as compared to an evaporation duct or a surface duct. This feature is attributed to the base layer of the surface-based duct, as shown in the MM5V3 curve of Fig. 6(b). The turbulence reduces the

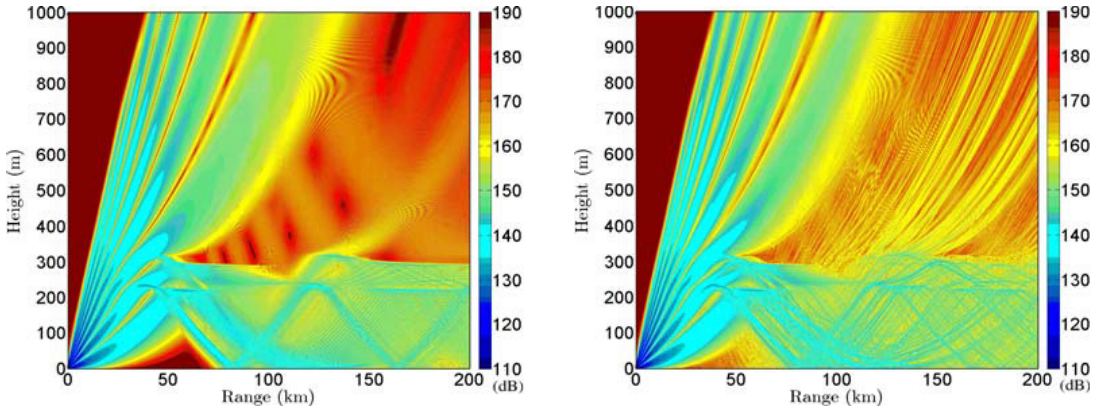

Figure 9. Distribution of path-loss in a stable ABL, with the parameters from —— curves in Figs. 6(b), 7, and 8(b), $z_t = 4\,\mathrm{m}$, $f = 10.6\,\mathrm{GHz}$; (a) without turbulence, (b) with turbulence.

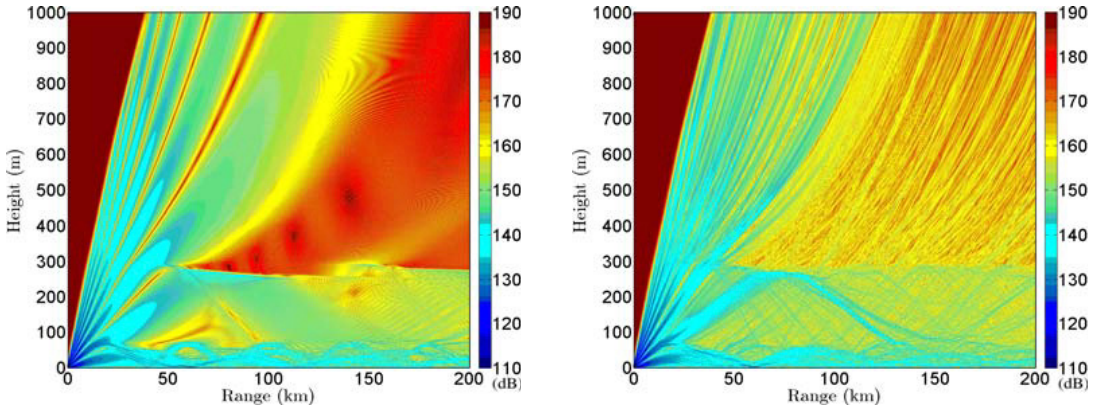

Figure 10. Distribution of path-loss in a stable ABL, with the parameters from —○— curves in Figs. 6(b), 7, and 8(b), $z_t = 4\,\mathrm{m}$, $f = 10.6\,\mathrm{GHz}$; (a) without turbulence, (b) with turbulence.

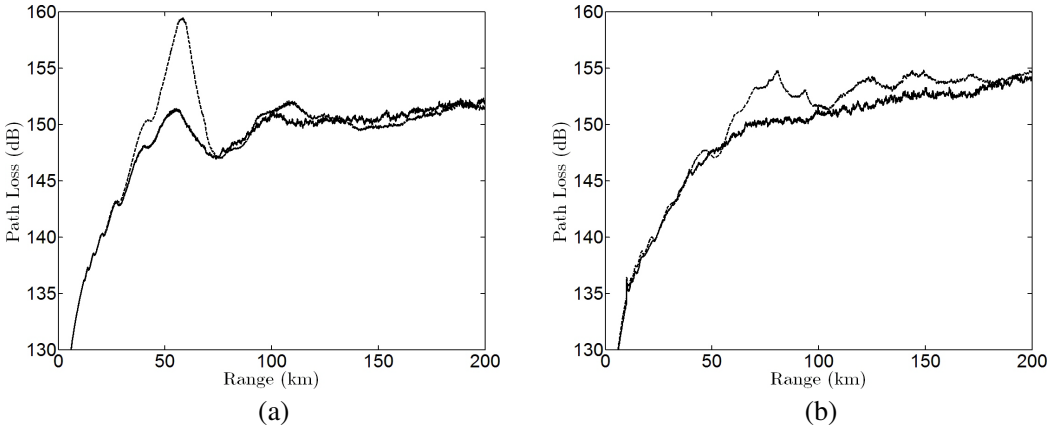

Figure 11. Average path-loss within duct, – – –: without turbulence, ——: with turbulence; (a) data from Fig. 9, with $z < 300\,\mathrm{m}$; (b) data from Fig. 10, with $z < 250\,\mathrm{m}$.

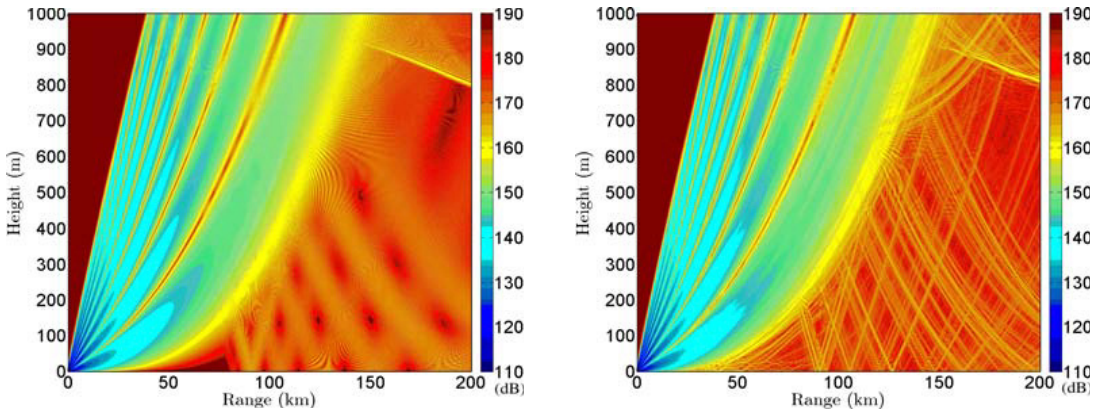

Figure 12. Distribution of path-loss in an unstable ABL, with the parameters from —△— curves in Figs. 6(b), 7, and 8(b), $z_t = 4\,\text{m}$, $f = 10.6\,\text{GHz}$; (a) without turbulence, (b) with turbulence.

path-loss in that shadowing region by about 10 dB.

In Fig. 10, a steady communication channel appears below 80 m due to the surface ducting layer of the complex duct, as shown in the rawinsonde curve of Fig. 6(b). The ducting effect is less obvious above 80 m, and a feeble duct appears below the height of 250 m. A shadowing region appears around the range of 30 to 80 km and the height of 100 m. The path-loss therein is reduced by about 5 dB in the presence of turbulence, although not so obvious as in Fig. 9.

In both Figs. 9 and 10, the turbulence seems to smear the border of duct, and the path-loss above the duct is generally reduced. In summary, significant turbulence effects are observed within the ducting region above the sea in daytime, under stable conditions, which can be attributed to the large refractive-index gradient. The energy leakage from the ducting to the non-ducting regions, caused by the turbulence, leads to a more uniform distribution of path-loss distribution within the duct.

Figure 11 shows the average path-loss within the duct, using the data in Figs. 9 and 10, respectively. It is observed that the turbulence effect reduces the variation of average path-loss over range.

Figure 12 shows distribution of path-loss in an unstable ABL without duct. The turbulence makes only little difference.

5. CONCLUSION

A complete model has been proposed to study wave propagation in an atmospheric boundary layer (ABL), in the presence of air turbulence. All the relevant parameters are estimated on the atmospheric conditions, with the scaling parameters derived from the measurement data. A systematic approach, based on split-step Fourier propagation algorithm, has also been developed to simulate wave propagation in atmospheric ducts, with proper range of parameters closely related to the weather condition of the ABL. A set of measurement data in the Gulf area is used to confirm the effectiveness of this approach.

ACKNOWLEDGMENT

This work was sponsored by the National Science Council, Taiwan, under contract NSC 100-2221-E-002-232; and the Ministry of Education, Taiwan, under Aim for Top University Project 103R3401-1.

REFERENCES

1. Mentes, S. S. and Z. Kaymaz, "Investigation of surface duct conditions over Istanbul, Turkey," *J. Appl. Meteorol. Climatol.*, Vol. 46, No. 3, 318–337, 2007.
2. Skolnik, M. I., *Introduction to Radar Systems*, 3rd edition, McGraw-Hill, 2001.

3. Ulaby, F. T., R. K. Moore, and A. K. Fung, "Microwave remote sensing fundamentals and radiometry," *Microwave Remote Sensing: Active and Passive*, Vol. 1, Addison-Wesley, 1981.
4. Kerans, A., A. S. Kulessa, E. Lensson, G. French, and G. S. Woods, "Implications of the evaporation duct for microwave radio path design over tropical oceans in Northern Australia," *Workshop Appl. Radio Sci.*, Leura, Australia, 2002.
5. Sirkova, I. and M. Mikhalev, "Parabolic-equation-based study of ducting effects on microwave propagation," *Microwave Opt. Technol. Lett.*, Vol. 42, No. 5, 390–394, 2004.
6. Sirkova, I. and M. Mikhalev, "Influence of tropospheric duct parameters changes on microwave path loss," *Proc. Int. Sci. Conf. Info. Commun. Energy Syst. Technol.*, 43–46, Sofia, Bulgaria, 2003.
7. Kuttler, J. R. and G. D. Dockery, "Theoretical description of the parabolic approximation/Fourier split-step method of representing electromagnetic propagation in the troposphere," *Radio Sci.*, Vol. 26, No. 2, 381–393, 1991.
8. Douchin, N., S. Bolioli, F. Christophe, and P. Combes, "Theoretical study of the evaporation duct effects on satellite-to-ship radio links near the horizon," *IEE Proc. Microwaves Antennas Propagat.*, Vol. 141, No. 4, 272–278, 1994.
9. Apaydin, G. and L. Sevgi, "FEM-based surface wave multimixed-path propagator and path loss predictions," *IEEE Antennas Wireless Propagat. Lett.*, Vol. 8, 1010–1013, 2009.
10. Essen, H. and H. H. Fuchs, "Microwave and millimeterwave propagation within the marine boundary layer," *German Microwave Conf.*, Karlsruhe, Germany, 2006.
11. Degrazia, G. A., D. Anfossi, J. C. Carvalho, C. Mangia, T. Tirabassi, and H. F. C. Velho, "Turbulence parameterisation for PBL dispersion models in all stability conditions," *Atmos. Environ.*, Vol. 34, No. 21, 3575–3583, 2000.
12. Kukushkin, A. and J. Wiley, *Radio Wave Propagation in the Marine Boundary Layer*, Wiley Online Library, 2004.
13. Rouseff, D., "Simulated microwave propagation through tropospheric turbulence," *IEEE Trans. Antennas Propagat.*, Vol. 40, No. 9, 1076–1083, 1992.
14. Hitney, H. V., "A practical tropospheric scatter model using the parabolic equation," *IEEE Trans. Antennas Propagat.*, Vol. 41, No. 7, 905–909, 1993.
15. Hitney, H. V., "Evaporation duct propagation and near-grazing angle scattering from a rough sea," *IEEE Int. Geosci. Remote Sensing Symp.*, 2631–2633, 1999.
16. Bein, G., "Monte Carlo computer technique for one-dimensional random media," *IEEE Trans. Antennas Propagat.*, Vol. 21, No. 1, 83–88, 1973.
17. Adams, R. N. and E. D. Denman, *Wave Propagation and Turbulent Media*, Elsevier, 1966.
18. Holtslag, A. A. M. and F. T. M. Nieuwstadt, "Scaling the atmospheric boundary layer," *Boundary Layer Meteorol.*, Vol. 36, No. 1, 201–209, 1986.
19. Kaimal, J. C., J. C. Wyngaard, D. A. Haugen, O. R. Cote, Y. Izumi, S. J. Caughey, and C. J. Readings, "Turbulence structure in the convective boundary layer," *J. Atmos. Sci.*, Vol. 33, No. 11, 2152–2169, 1976.
20. Moeng, C.-H., "A large-eddy-simulation model for the study of planetary boundary-layer turbulence," *J. Atmos. Sci.*, Vol. 41, No. 13, 2052–2062, 1984.
21. Nieuwstadt, F. T. M., "The turbulent structure of the stable, nocturnal boundary layer," *J. Atmos. Sci.*, Vol. 41, No. 14, 2202–2216, 1984.
22. Levy, M., *Parabolic Equation Methods for Electromagnetic Wave Propagation*, Inst. Electr. Eng., 2000.
23. Frehlich, R., "Simulation of laser propagation in a turbulent atmosphere," *Appl. Opt.*, Vol. 39, No. 3, 393–397, Jan. 2000.
24. Wiener, N., "Generalized harmonic analysis," *Acta Mathematica*, Vol. 55, No. 1, 117–258, 1930.
25. Ishimaru, A., *Wave Propagation and Scattering in Random Media*, IEEE Press, 1997.
26. Fabbro, V. and L. Féral, "Comparison of 2D and 3D electromagnetic approaches to predict tropospheric turbulence effects in clear sky conditions," *IEEE Trans. Antennas Propagat.*, Vol. 60, No. 9, 4398–4407, 2012.

27. Smith, E. K. and S. Weintraub, "The constants in the equation for atmospheric refractive index at radio frequencies," *Proc. IRE*, Vol. 41, 1035–1037, 1953.
28. Bean, B. R. and E. Dutton, *Radio Meteorology*, Dover Publications, 1968.
29. Berberan-Santos, M. N., E. N. Bodunov, and L. Pogliani, "On the barometric formula," *Am. J. Phys.*, Vol. 65, 404, 1997.
30. Wallace, J. M. and P. V. Hobbs, *Atmospheric Science: An Introductory Survey*, Academic Press, 2006.
31. Arya, P. S., *Introduction to Micrometeorology*, 2nd edition, Academic press, 2001.
32. Yamartino, R. J., J. S. Scire, G. R. Carmichael, and Y. S. Chang, "The CALGRID mesoscale photochemical grid model. I. Model formulation," *Atmos. Environ. Part A*, Vol. 26, No. 8, 1493–1512, 1992.
33. De Bruin, H. A. R., R. J. Ronda, and B. J. H. Van De Wiel, "Approximate solutions for the Obukhov length and the surface fluxes in terms of bulk Richardson numbers," *Boundary Layer Meteorol.*, Vol. 95, No. 1, 145–157, 2000.
34. Panovsky, H. A. and J. A. Dutton, *Atmospheric Turbulence: Models and Methods for Engineering Applications*, John Wiley, 1984.
35. Seibert, P., F. Beyrich, S.-E. Gryning, S. Joffre, A. Rasmussen, and P. Tercier, "Review and intercomparison of operational methods for the determination of the mixing height," *Atmos. Environ.*, Vol. 34, No. 7, 1001–1027, 2000.
36. Gryning, S.-E. and E. Batchvarova, "Parameterization of the depth of the entrainment zone above the daytime mixed layer," *Quart. J. Royal Meteorol. Soc.*, Vol. 120, No. 515, 47–58, 1994.
37. Sun, J., W. Jiang, Z. Chen, and R. Yuan, "Parameterization for the depth of the entrainment zone above the convectively mixed layer," *Adv. Atmos. Sci.*, Vol. 22, No. 1, 114–121, 2005.
38. Cox, D. C., H. W. Arnold, and H. H. Hoffman, "Observations of cloud-produced amplitude scintillation on 19- and 28-GHz Earth-space paths," *Radio Sci.*, Vol. 16, No. 5, 885–907, 1981.
39. Tunick, A., "Optical turbulence effects on ground to satellite microwave refractivity," DTIC Document ADA449682, 2006.
40. Andreas, E. L., "On the Kolmogorov constants for the temperature-humidity cospectrum and the refractive index spectrum," *J. Atmos. Sci.*, Vol. 44, No. 17, 2399–2406, 1987.
41. Tatarskii, V. I., *The Effects of the Turbulent Atmosphere on Wave Propagation*, Israel Program for Scientific Translations, 1971.
42. Burk, S. D., "Refractive index structure parameters-time-dependent calculations using a numerical boundary-layer model," *J. Appl. Meteorol.*, Vol. 19, 562–576, 1980.
43. Gryning, S. E., E. Batchvarova, B. Brümmer, H. Jørgensen, and S. Larsen, "On the extension of the wind profile over homogeneous terrain beyond the surface boundary layer," *Boundary Layer Meteorol.*, Vol. 124, No. 2, 251–268, 2007.
44. Brooks, I. M., A. K. Goroch, and D. P. Rogers, "Observations of strong surface radar ducts over the Persian Gulf," *J. Appl. Meteorol.*, Vol. 38, No. 9, 1293–1310, 1999.
45. Atkinson, B. W. and M. Zhu, "Radar-duct and boundary-layer characteristics over the area of the Gulf," *Q. J. R. Meteorol. Soc.*, Vol. 131, No. 609, 1923–1953, 2005.
46. Rao, P. G., H. R. Hatwar, M. H. Al-Sulaiti, and A. H. Al-Mulla, "Summer shamals over the Arabian Gulf," *Weather*, Vol. 58, No. 12, 471–478, 2003.
47. Garratt, J. R. and B. F. Ryan, "The structure of the stably stratified internal boundary layer in offshore flow over the sea," *Boundary-Layer Meteorol.*, Vol. 47, No. 1, 17–40, 1989.
48. Plant, R. S. and B. W. Atkinson, "Sea-breeze modification of the growth of a marine internal boundary layer," *Boundary Layer Meteorol.*, Vol. 104, No. 2, 201–228, 2002.
49. Zhu, M. and B. W. Atkinson, "Observed and modelled climatology of the land-sea breeze circulation over the Persian Gulf," *Int. J. Climatol.*, Vol. 24, No. 7, 883–905, 2004.
50. Lüdi, A. and A. Magun, "Near-horizontal line-of-sight millimeter-wave propagation measurements for the determination of outer length scales and anisotropy of turbulent refractive index fluctuations in the lower troposphere," *Radio Sci.*, Vol. 37, No. 2, 12-1–19, 2002.